Ashish Yadav

Materials Chemistry and Physics 297 (2023) 127444

Contents lists available at ScienceDirect

Materials Chemistry and Physics

journal homepage: www.elsevier.com/locate/matchemphys

Influence of ionic radii on the conduction mechanism in lanthanum silicate oxyapatite

Ashishkumar Yadav [a,b], Priyanka A. Jha [a,*], Pardeep K. Jha [a], Neetu Jha [c], Prabhakar Singh [a,**]

[a] Department of Physics, Indian Institute of Technology (Banaras Hindu University) Varanasi, Varanasi, 221005, India
[b] R.J. College, University of Mumbai, Ghatkopar, Mumbai, 400086, India
[c] Department of Physics, Institute of Chemical Technology Mumbai, 400019, India

HIGHLIGHTS

- Compositional effect of Ca and Ba in $(La_{1-x}A_x)_{9.67}(SiO_4)_6O_{2+\delta}$ is studied.
- The conductivity is higher in Ca substituted sample than Ba substituted sample.
- Ion mobility volume has risen 3 times in Ca substituted sample than Ba substituted.
- s-p interaction is playing a critical role in the conduction of Ca substituted sample.
- Loss is occurring due to s-d interaction in Ba substituted sample.

ABSTRACT

Lanthanum Silicate oxyapatite has attracted researchers due to its interesting ion channels and conduction pathways. In the present work, the average ionic radii of La site are altered via substitution of La^{3+} with Ba^{2+} and Ca^{2+} to form $(La_{1-x}A_x)_{9.67}(SiO_4)_6O_{2+\delta}$ ($x = 0.0$, 0.05, 0.10 and 0.15) where A = Ca and Ba. Further, the ionic radii of substituents will alter the average area of critical triangle (saddle point). Therefore, it is expected to affect the ion mobility. The single-phase Ca and Ba substituted samples are observed and Rietveld refinement suggests no phase change with the ionic radii. The elemental content obtained from Rietveld refinement, Energy dispersion spectra, X-ray photoelectron spectroscopy and thermogravimetric analysis suggests La deficiency in Ca substituted sample and O deficiency in Ba substituted sample. Temperature and frequency dependent ac conductivity in the temperature range (548 K–973 K) suggests that the conductivity is higher at $x = 0.05$ than $x = 0.1$ in Ba substituted sample. On a comparative note, the conductivity is higher in Ca substituted sample than that of the Ba substituted sample for $x = 0.1$.

1. Introduction

Oxide ion conductors (OICs) have attracted researchers due to their significant role in electrochemical conversion devices (solid oxide fuel cell (SOFC)) [1]. SOFC is a technology helping to solve the current energy problems i.e., supply and demand by providing a solution to environmental pollution [2,3]. Here the recent increase in demand has come from the domestic sector which requires low temperature fuel cells. For this, low temperature oxide ion conductors working in the temperature range (500 K–800 K) will be helpful in designing low temperature electrochemical solid oxide fuel cells [4]. High temperature (>1100 K) fast oxide ion conductors cannot work due to the sharp decrease in conductivity with temperature. Hence, oxide ion conductors in the low temperature and intermediate temperature (800 K–1100 K) are required.

Recently, apatite type rare earth silicates (discovered by Nakayama in 1995 [5]) have attracted the researchers due to their low activation energy in the ionic conduction [6]. Thus, they prove their suitability to work in the intermediate temperature range. Various synthesis techniques have been employed from the c-axis orientation and porosity optimization and in turn, their effects on conductivity. The nanostructuring of these compounds is still in infant stage and more work is required from the researchers. Moreover, porous network is obtained in these compounds with the formation of lanthanum nanodomains [7]. However, sol-gel technique is used to synthesize spherical nanoparticles [8] but their conductivity is not yet studied.

Among these OICs, lanthanum silicate oxyapatite i.e., $La^{3+}_{10-\alpha}(SiO_4)^{4-}_6O^{2-}_{2+\delta}$ (LSO) is one of the most interesting materials due to

* Corresponding author.
** Corresponding author.
E-mail addresses: priyankajha.dce@gmail.com (P.A. Jha), psingh.app@iitbhu.ac.in (P. Singh).

https://doi.org/10.1016/j.matchemphys.2023.127444
Received 17 October 2022; Received in revised form 16 January 2023; Accepted 25 January 2023
Available online 26 January 2023

its anisotropic ion conduction [9,10]. Further, conduction via vacancy diffusion mechanism of oxygen ion through interstitials is proposed for the materials [11–13]. Its hexagonal structure possesses an array of oxygen ions along c-axis, lanthanum ions surrounding the oxygen ions, SiO_4 cluster and another lanthanum in between the clusters [14–17]. In the structure lanthanum vacancies are included in order to maintain charge neutrality and oxygen conduction along c-axis takes place [18, 19]. Furthermore, it is expected to be modified with the substitution. Thus, there is scope of conductivity enhancement in polycrystalline LSO with grain alignment (i.e. $(\sigma_c^{\parallel} / \sigma_c^{\perp} > 10$ i.e., conductivity in direction of grains parallel to c-axis is ten times larger than conductivity in direction of grains perpendicular to c-axis)) [9,10] and doping [20,21].

There are studies claiming that oxygen interstitial, O_i, is the dominant charge carrier for conduction rather than typical oxygen vacancies with a diffusion barrier of 0.5–0.8 eV [22,23]. This barrier accounts for the contribution of lanthanum vacancy as well [24]. If lanthanum vacancy can be reduced then this barrier might reduce. Lanthanum vacancy are created by charge balance and their concentration is maintained by aliovalent elemental substitution [25] as in the case of perovskites [26,27]. Various doping such as Al, Mg at B-site [20] and Alkaline earth [16,21,28–31] and rare earth substitutions at A-site [25] have been done in order to stabilise their structure and change the conduction mechanism viz. push pull and interstitial are well described for the oxyapatite but its dynamics is still scarce. Further, substitution can bring some unusual thermodynamics and possibility of altered defect-formation is quite possible [32]. Thus, the effect of ionic radii on the structural and dynamics disorder in parent $La^{3+}_{10-\alpha}(SiO_4)^{4-}_6O^{2-}_{2+\delta}$ and substituted $(La_{1-x}A_x)_{10-\alpha}(SiO_4)_6O_{2+\delta}$ (x = 0.0, 0.05, 0.10 and 0.15) where A = Ca and Ba compounds is studied via structural, electrical, optical and thermal studies.

1.1. Composition selection

The ionic conductivity depends on the product of occupancy of oxygen ion and its vacancy. Further, the creation of oxygen vacancies in case of apatite's depends upon lanthanum content. For this, we define two parameters δ, (+ve value represents oxygen excess and -ve value represents oxygen deficiency) and α, lanthanum deficiency. La can be substituted with divalent metals, A. Further, the composition can be defined with the help of eqn (1).

$$(5-x)La_2O_3 + xACO_3 + 6SiO_2 \rightarrow La_{10-x-\alpha}A_xSi_6O_{26+\delta} + xCO\uparrow + (x+1/2)O_2\uparrow + \alpha V^{3+}_{La} + \delta V^{2-}_{O} \quad (1)$$

It can be seen that CO and O_2 gas are evacuated with the formation of La and O vacancies. The interrelation between La vacancies (in terms of α) and O vacancies (in terms of δ) with aliovalent substitution at La-site (in term of x) are pictorially represented as Fig. 1 by fixing some values of α and x in equation (1). It can be seen that when α = 1, with the increase in x, δ is -ve. In this region, the probability of formation of secondary phase increases. When α = 0, with the increase in x, δ decreases but will always be +ve. In this regime, sample will be more electronic. For α = 0.5, the substitution limit reduces to x = 0.05. For α = 0.67 and 0.33, it can be seen that for x > 0.1, oxygen vacancy formation is more as compared to oxygen vacancy formation for x < 0.1. However, at x = 0.1, La content and O vacancy are quite balanced. That's why, these two are the major choice of α. Here, in the present work, α = 0.33 is chosen and varied x up to 0.15 at the steps of 0.05 on the basis of charge neutrality.

Till now the charge compensation is only considered while the role of ionic radii is ignored. However, the ionic radius of substituents is pivotal parameter as it alters the average area of critical triangle (saddle point)

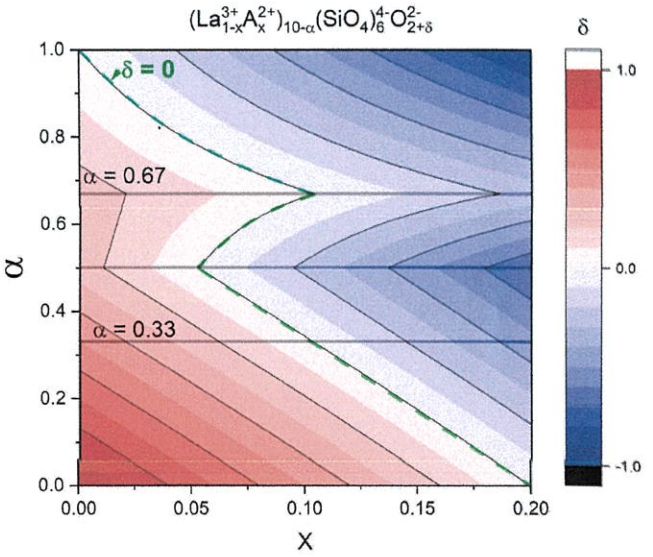

Fig. 1. Variation of La content with O vacancies on varying x.

significantly and therefore ion mobility. Here 'A' can be Ba, Sr and Ca and their ionic radii vary in the order of Ca (134 p.m.) > Sr (144 p.m.) > Ba (161 p.m.) with 12 coordination number. Fig. 2 depicts the higher ion mobility volume (V_{IM}) for Ca substituted samples than Sr and Ba substituted samples i.e., with the increase in ionic radii ($<R_{i,\,La}>$) from Ca to Ba, ion mobility decreases. Moreover, it is also observed that with the increase in x of Ca, $<R_{i,\,La}>$ decreases and with the increase in Ba content, $<R_{i,\,La}>$ increases (Fig. 2 (inset)).

2. Materials and methods

2.1. Sample preparation

Apatite based material $(La_{1-x}A_x)_{10-\alpha}(SiO_4)_6O_{2+\delta}$ (x = 0.0, 0.05, 0.10 and 0.15) where A = Ca and Ba were prepared using solid state route method. The constituent materials La_2O_3 (Sigma-Aldrich 99.9%), SiO_2 (Sigma-Aldrich 99.5%), $CaCO_3$ (99%) and $BaCO_3$ (99%) were weighed stoichiometrically and thoroughly ground using mortar and pestle for 30–40 min. The obtained powder was then ground in ball-mill with propanol using zirconia ball and vial for 6 h maintaining the powder to ball weight ratio. The ball milled powder was calcined at 1000 °C for 8 h and phase determination of the calcined powder was done. Further, calcined powder was then ground and mixed with Polyvinyl alcohol (PVA) as a binder and pressed at 7 MPa to turn for pelletization and pellets were then sintered at 1375 °C for 14 h at the heating rate of 5 ^{o}Cmin $^{-1}$.

2.2. Characterization techniques

The phase identification of calcined powder and sintered pellets was done through Rigaku Miniflex powder diffractometer with Cu- Kα radiation (λ = 1.540598 Å) and Ni filter in the range 2θ ~ 20 - 80° with a step size of 0.02°. The XRD data was refined with $P6_{3/m}$ symmetry using Full Prof Suite software package in structural Rietveld mode. After applying zero correction of the instrument, Pseudo - Voigt peak profile was used for refinement. The structure is studied using Diamond 3.0

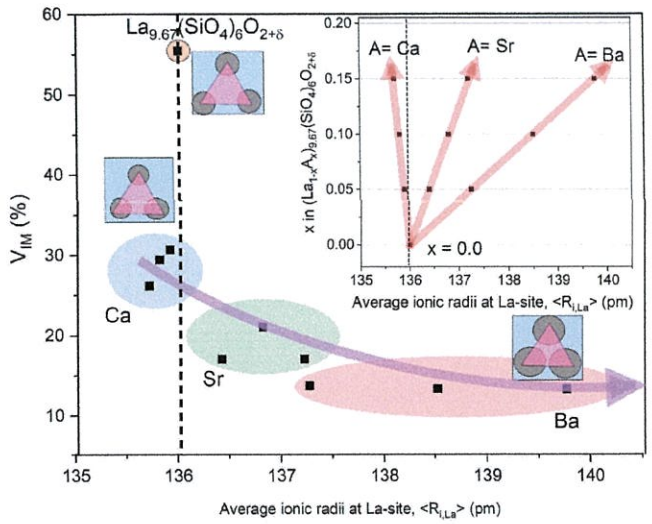

Fig. 2. Variation of ion mobility volume with average ionic radii at La site as average ionic radii varies from Ca to Ba with the increase in their respective contents (inset) depicts the variation of ionic radii with the variation on Ba, Sr and Ca concentrations.

software and bond distances along with lattice parameters are obtained. Further, bond valence sum (BVS) calculation is done using Full Prof software to find the percolation energy. The thermogravimetric analysis of the calcined powders was carried out simultaneous TG-DSC (Mettler Toledo, Germany) thermal analyzer in the temperature range 30–1000 °C at a constant heating rate of 10 °Cmin $^{-1}$ in the nitrogen atmospheres. The density of prepared sintered pellet was measured using density kit (Sartorius, BSA2245CW). The elemental compositions (EDAX) of the sintered pellets were characterized using scanning electron microscopy (EVO - Scanning Electron Microscope MA15/18). The *average grain size was calculated using the linear intercept method. The* electrical measurements were done using LCR meter (Wayne Kerr 6500P) in the temperature range 100 °C–700 °C over the frequency range of between 20 Hz and 1 MHz. The elemental composition was further verified using X-ray photoelectron spectroscopy (Kratos Amicus model) high performance analytical instrument utilizing Mg target under 10−^{6} Pa pressure. The UV–VIS absorption spectra was taken by JASCO V-770 ultraviolet–visible (UV) spectrometer.

3. Results and analysis

The single phase $(La_{1-x}A_x)_{10-\alpha}(SiO_4)_6O_{2+\delta}$ (x = 0.0, 0.05, 0.10 and 0.15) where A = Ca and Ba compounds are obtained using solid state reaction route. The Rietveld refined X-ray diffractograms are shown in supplementary as Figs. S1 and S2. The lattice parameters, bond lengths, Wyckoff positions and occupancy for both the substituents Ba and Ca are shown in Fig. S3-S4, Table S1 and Table S2, respectively. The conductivity-frequency -temperature (σ - ω -T) (10 s $^{-1}$ < ω ≤ 10^{6} s $^{-1}$) dependent plots (548–973 K) (Fig. S5) are fitted with Jonscher Power law (JPL) [33] and the fitting parameters dc conductivity (σ_{dc}), hopping frequency (ω_h) and exponent (p) are extracted

$$\sigma = \sigma_{dc}(1 + (\omega/\omega_h)^p) \quad (2)$$

3.1. Temperature dependence conduction behaviour

3.1.1. dc conductivity

Fig. 3 depicts σ_{dc} -T plot for Ba and Ca substituted samples and it can be seen that in Ba substituted samples, conductivity is higher at x = 0.05 than the parent sample there after it decreases for x ≥ 0.1. However, for Ca substituted samples, conductivity increases up to x = 0.1 with x there after it decreases for x = 0.15. Further, σ_{dc} -T curves are fitted with nearest neighbour hopping (NNH) model [34,35] σT = σ_0 exp (-E_a/k_BT) (individual colour lines). For T > 750 K fitting lines match well with the data but for T < 750 K fitted lines don't match well with the data. Further, the conductivity is observed to be higher for x = 0.1 in Ca substituted samples in comparison to the Ba substituted samples.

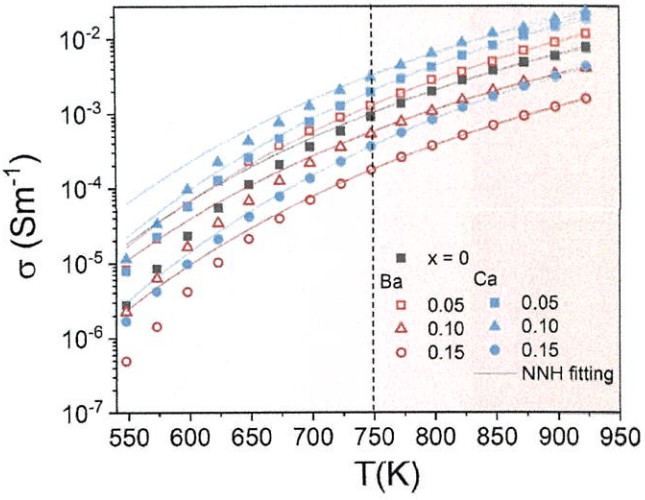

Fig. 3. σ_{dc} -T plot for Ba and Ca substituted samples with nearest neighbour hopping.

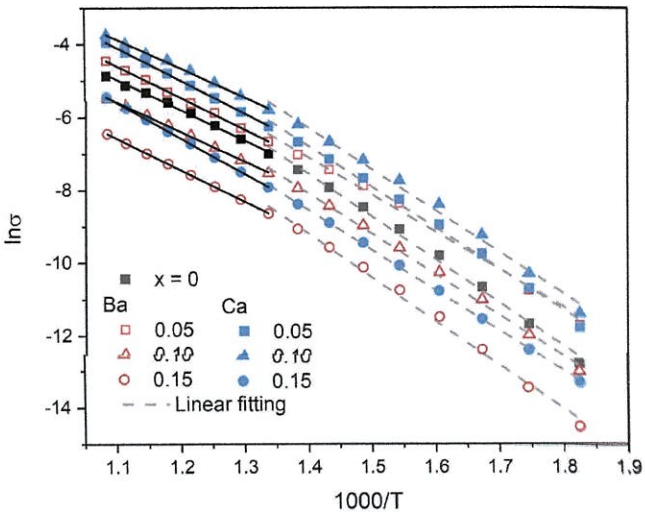

Fig. 4. Arrhenius plots for Ca ad Ba substituted $(La_{1-x}A_x)_{10-\alpha}(SiO_4)_6O_{2+\delta}$ (x = 0.0, 0.05, 0.10 and 0.15).

The deviation of fitted lines from the data points suggested to fit the data points in the two regimes. Fig. 4 depicts the Arrhenius plots in the two regimes and activation energies are estimated in the two regimes for *all the samples. Most importantly, we have observed two slopes* in the parent as well as substituted samples. The silicates are well known for high temperature (T ~ 1273 K) and pressure phase transitions (P ~ 20 GPa); therefore, phase transition could not be the reason for the observed two slopes near 700 K [36,37]. Another possibility is the extrinsic contribution as the conductivity spectra comprises of intrinsic, extrinsic and exhaustion regions with temperature, these regions occur due to difference of defect creation in the different temperature regimes and these defect centres donate the electrons to the conduction band [38,39]. Thus, conductivity for T < 700 K is [illegible] ionized leading to energy E d/2. The conductivity lowers for T < 700 K due to the slow

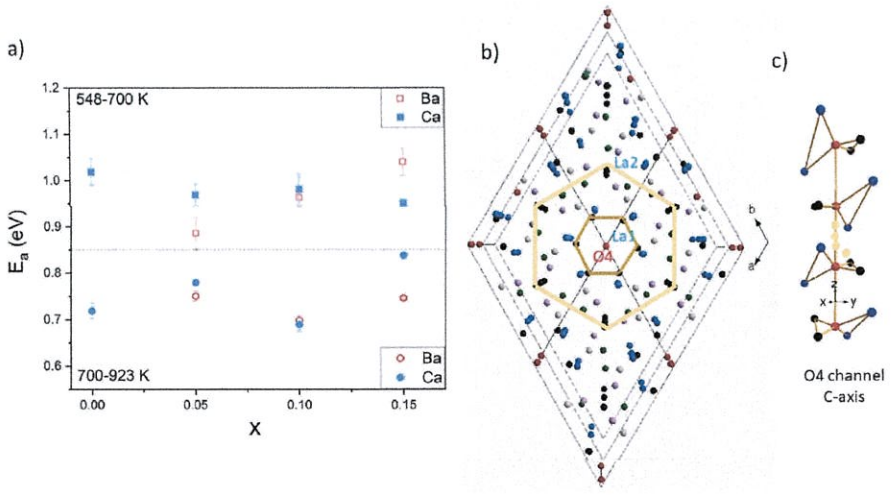

Fig. 5. Activation energies for Ca ad Ba substituted $(La_{1-x}A_x)_{10}$. $_\alpha(SiO_4)_6O_{2+\delta}$ (x = 0.0, 0.05, 0.10 and 0.15) and (b) shows the structure for the movement of interstitial oxygen vacancies, La1 and La2 form concentric hexagons in a-b plane with O4 in centre and (c) channel formed by O4 along c-axis.

movement of charge carriers. Further, for T > 700 K, donation of electrons to the conduction band via defects increases the conductivity. To understand this in a better way, grain, grain-boundary contributions are analysed in detail.

The activation energies estimated in the two regimes are illustrated here (Fig. 5(a)) and it is observed that E_a in the range of 0.9–1.1eV for T < 700 K. Further, for T > 700 K, E a lies in the range of 0.7–0.85 eV. This is in further correlation with the DFT studies suggesting the formation of oxygen vacancies and moving to interstitial sites [32,40]. Fig. 5(b) shows the structure for the movement of interstitial oxygen vacancies, La1 and La2 form concentric hexagons in a-b plane with O4 in centre and further O4 forms a channel along c-axis as shown in Fig. 5(c). Further, if any Frenkel defect would have been created with oxygen vacancy then activation energy would have risen to 4 eV [40]. Thus, in the present case, activation energy suggests thermally activated conduction via oxygen vacancies. Further, activation energy is not changing significantly with the ionic radii. Now, coming to the main observation why the better conductivity is observed for Ca (x = 0.1) than Ba (x = 0.1) which is contradictory to the literature [21]. Hereafter, a comparative of the two compositions with x = 0.1 is studied to find the reason for higher conduction in Ca substituted samples.

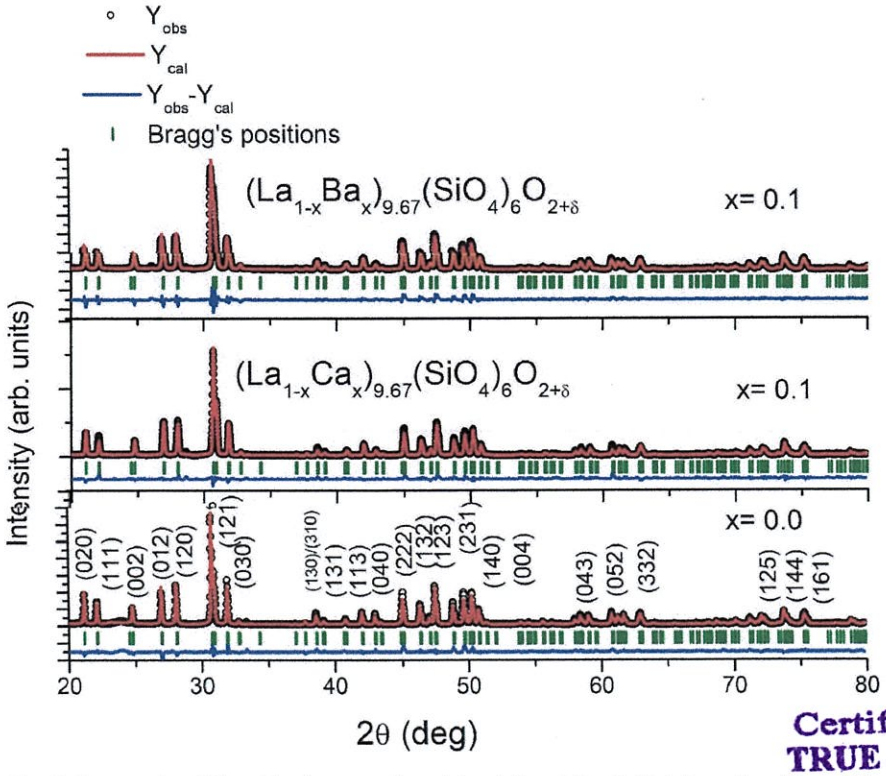

Fig. 6. Comparative of Rietveld refinement of x = 0.0 and Ca and Ba substituted samples with x = 0.1.

3.2. Why Ca substitution is better than Ba substitution?

Fig. 6 shows the Rietveld refined X-ray diffractograms of the parent, Ba and Ca substituted samples with x = 0.1. The refinement is done with P6 3/m symmetry using Full Prof Suite package after applying instrumental correction and Pseudo-Voigt peak profile. However, the supplementary shows the detailed refinement and parameters as Figs. S1–S4 and Tables S1 and S2. The goodness of fit ($\chi^2 < 2.5$ [41,42]) is also mentioned in Figs. S1(a) and S2(a). The single-phase Ba substituted lanthanum silicate samples are observed for x < 0.15 whereas for x = 0.15, a secondary phase at $2\theta \approx 33°$ corresponding to BaO is observed (JCPDS file No. 01–0746). In comparison to Ba substituted samples, secondary phase corresponding to SiO_2 is observed in Ca substituted samples. Further in Ba substituted samples, the peak splitting corresponding to $2\theta \approx 32°$ doesn't completely disappear but reduces with the increase in x (Fig.S1 b). However, on a comparative note, splitting disappears in Ca substituted samples. Further, the lattice parameters and ion mobility volume using bond valence sum calculations have been illustrated in Figs. S3–S4 for the Ba and Ca substituted samples.

It can be seen from Fig. 7 that on a comparative note, the dense grains with minimal porosity are observed for Ca substituted sample. Further, for Ba substituted sample, x = 0.1, smaller grains with porosity are observed. However, the grains are hexagonal in shape for Ba and Ca substituted samples. The morphology changes and grain size alteration with x are shown in Supplementary Fig. S6 and Fig. S7. Further, to determine the elemental concentration XPS, EDX and TGA are used.

A gradual mass loss is observed in Thermogravimetric (TGA) curves for all studies samples i.e., $(La_{1-x}A_x)_{9.67}(SiO_4)_6O_{2+\delta}$ where x = 0.0, 0.05, 0.10 and 0.15 with A = Ba and Ca (For details see supplementary (Figs. S8–S9)). Here, for a comparative purpose, TGA for x = 0.0, x = 0.1 Ba and x = 0.1 Ca substituted samples are shown in Fig. 8. In the parent sample, kinks correspond to the weight loss due to La. While with Ba substitution, these kinks correspond to the weight loss due to CO and O_2 as the weight loss observed in both the kinks are nearly 6% and 0.43% correspond to that of CO and O_2. For Ca modified system i.e., $(La_{1-x}Ca_x)_{9.67}(SiO_4)_6O_{2+\delta}$ (x = 0.0, 0.05, 0.10 and 0.15), there is a gradual mass loss and weight loss observed in is ~ 5.8% and matches the weight loss due to La. This suggests the formation of O deficient Ba substituted samples and La deficient parent and Ca substituted samples. The La and O deficiency observed is in accordance with the La content estimated from Rietveld refinement. In order to verify elemental content, XPS spectra (Fig. 9) has been deconvoluted.

The La 3d spectrum shows three chemical states corresponding to La_2O_3, $La(OH)_3$ and La_2CO_3 with well-defined and separated spin components and energies (ΔE, spin orbit splitting) corresponding to 4.6 eV, 3.9 eV and 0.3.5 eV, respectively. In Ca substituted sample, ΔE ~ 4.0eV corresponding to the spin orbit splitting corresponding to $La(OH)_3$ i.e. La^{3+} state is observed. In Ba substituted sample, ΔE ~ 3.5 eV corresponding to the spin orbit splitting corresponding to La_2CO_3 is observed. In Ca2p spectra (<1eV), chemical shift with the increase in x is observed (Fig. S10 and variation of Ba spectra with x is shown in Fig. S11). Further, Ca2p has spin orbit components with ΔE ~ 3.5eV.

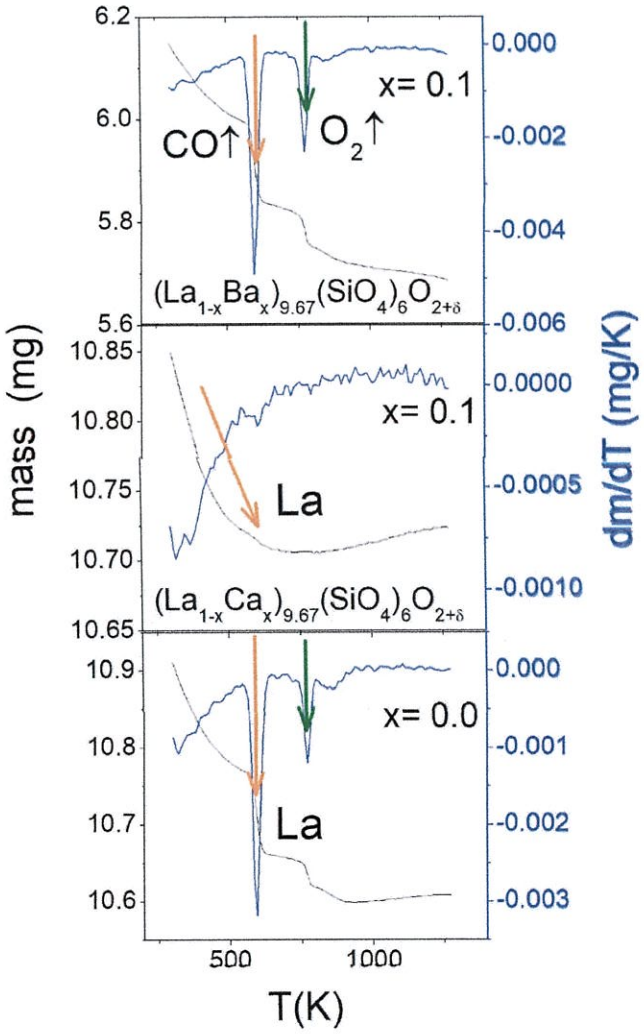

Fig. 8. TGA for x = 0.0, x = 0.1 Ba and x = 0.1 Ca substituted samples in $(La_{1-x}A_x)_{9.67}(SiO_4)_6O_{2+\delta}$.

Here, shake-up satellite is also observed but it cannot be resolved into its components as standard ones. In Ba 3d spectra, Ba loss peak is merged with the $3d_{3/2}$ peak affecting the O content (s-d interaction). Si 2p spectrum exhibits ΔE ~ 0.63 eV i.e., very close spin orbit splitting. Thus, asymmetric peaks corresponding to Si 2p i.e., Si^{4+} state are observed. Further, the intensity of Si $2p_{3/2}$ content is higher in Ca substituted sample than the parent and Ba substituted sample. In O spectra, O 1s peak at ~ 529 eV is linked to the metal and O bond (La–O, Si– O and Ca–O) while, 2nd peak of O belongs to metal-OH bond. Oxygen vacancy concentration is linked to the ratio of peak area corresponding to the M

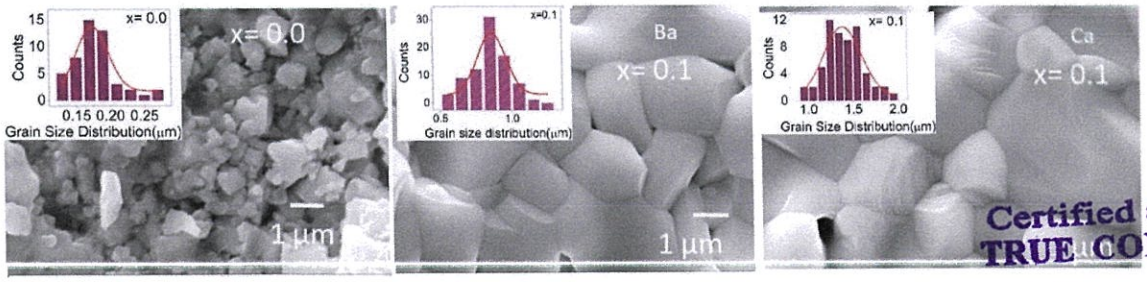

Fig. 7. Variation of grain size and morphology with x for parent and Ca and Ba substituted samples.

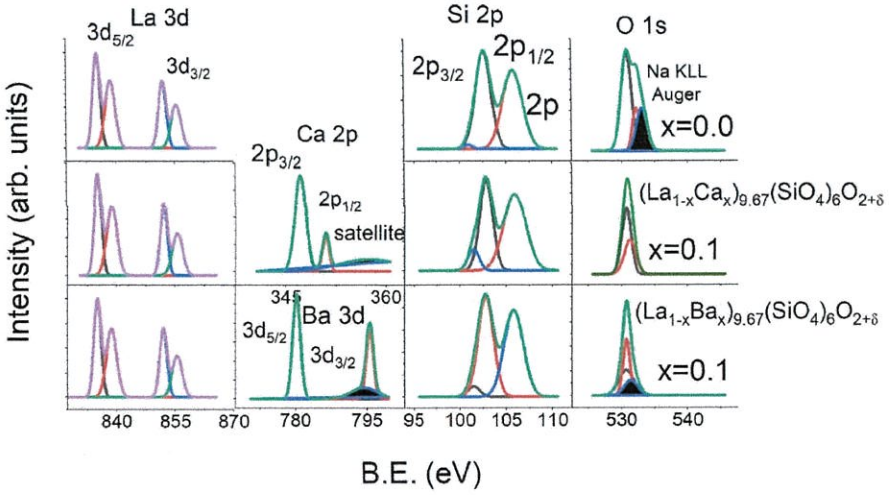

Fig. 9. Deconvoluted XPS spectra corresponding to La, Ba, Ca, Si and O for x = 0.0, x = 0.1 Ba and x = 0.1 Ca substituted samples in $(La_{1-x}A_x)_{9.67}(SiO_4)_6O_{2+\delta}$.

– O and M – OH bond. The intensity of M – OH peak is higher in Ba substituted sample rather than the parent and Ca substituted sample, Further, Na KLL Auger peak is observed in x = 0.0 and in Ca substituted sample, Auger peak diminishes. But in Ba substituted sample, Auger peak do not diminish. The occurrence of satellite peak in Ca 2p spectra and disappearance of Auger peak in O 1s spectra is due to metal ligand interaction i.e., interaction of s- orbital of Ca and p-orbital of O (s-p interaction). In addition, the formation of $La(OH)_3$ in Ca substituted sample suggests the formation of La vacancies and the samples are found to be La and Si deficient from the occupancies observed from the Rietveld refinement. On a comparative note, Ba substituted samples are more oxygen deficient due to the formation of La_2CO_3. Further, elemental content has been estimated from XPS and EDX (shown in supplementary, Fig. S12).

It is observed in Fig. 10 (a) that grain size (obtained from grain size histograms) is increasing with x with an exception at x = 0.15 in Ca substituted samples and grain size increases with x in Ba substituted samples. In Ca substituted samples, the trend of grain size is similar to the trend in La content (Fig. 10(b)). Further, Si and O are behaving opposite to each other i.e., with the increase in x Si content increases (Fig. 10(c)) and O content decreases (Fig. 10(d)). In Ba substituted samples, the trend of grain size is similar to the trend in O content. Here, (La + Ba) and Si content have no definite trend with x. Thus, this result is in accordance with the La deficiency for Ca substituted and O deficiency for Ba substituted samples. This can be understood as follows. The formation of $La(OH)_3$ suggests the formation of La vacancies and the samples are found to be La and Si deficient from the occupancies observed from the Rietveld refinement in Ca substituted sample with the higher ion mobility volume. The formation of $LaCO_3$ suggests the formation of O vacancies and the samples are found to be O deficient from the occupancies observed from the Rietveld refinement in Ba substituted sample with the lower ion mobility volume.

Fig. 11 shows plot of Z′ vs Z′′ (Nyquist plots) taken over a wide frequency range (20 Hz–1 MHz) at different temperatures *(400 °C–650 °C) for* $(La_{1-x}A_x)_{9.67}(SiO_4)_6O_{2+\delta}$ *system (a)* x = 0.0 (b) x = 0.1 with A = Ba, and (c) x = 0.1 with A = Ca, (d) zoomed portion of Nyquist plot at high temperatures (575 °C–650 °C). The depressed semicircles with off-centring on x-axis indicating non- Debye behaviour are observed. However, two semicircles in the Nyquist plots are observed for parent and Ba substituted sample indicating the presence of

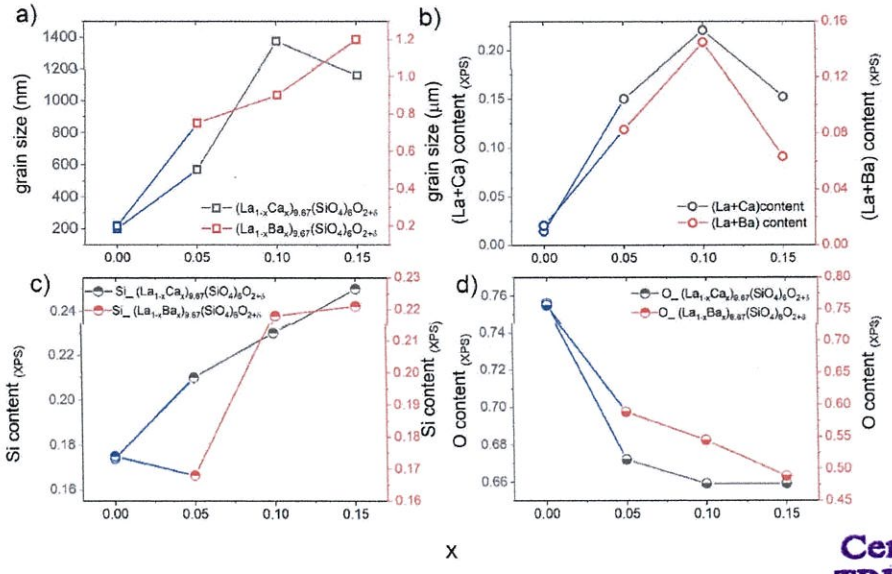

Fig. 10. (a) Grain size obtained from SEM micrographs (grain histograms) for Ca and Ba substituted samples (b) La + Ba content extracted from XPS, La + Ca content extracted from XPS (c) Si content from XPS (d) O content from XPS (lines are a guide to eye).

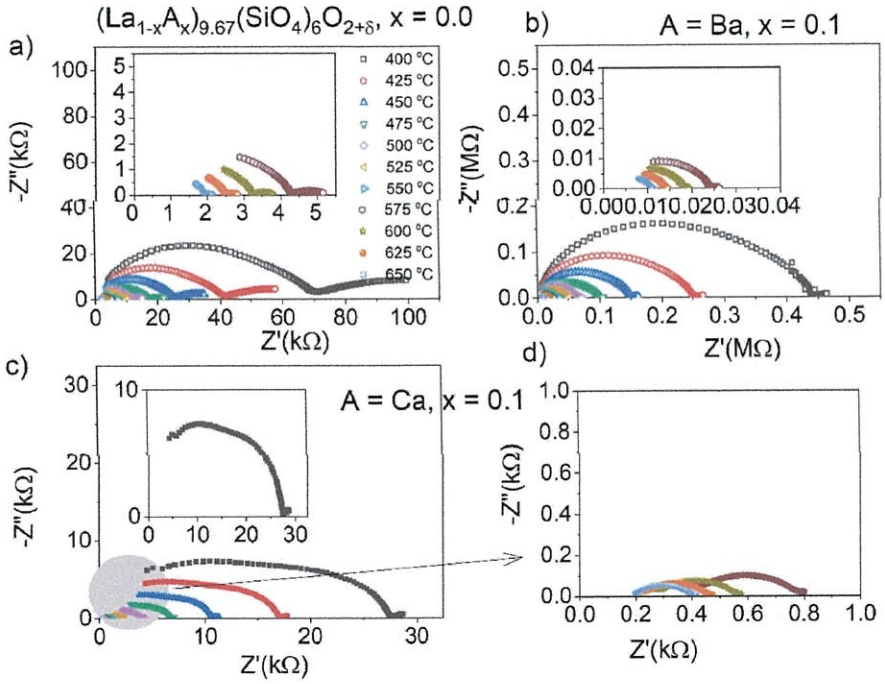

Fig. 11. Nyquist plots taken over a wide frequency range (20 Hz–1 MHz) at different temperatures (400 °C–650 °C) for $(La_{1-x}A_x)_{9.67}(SiO_4)_6O_{2+\delta}$ system (a) x = 0.0 (b) x = 0.1 with A = Ba, and (c) x = 0.1 with A = Ca, (d) zoomed portion of Nyquist plot at high temperatures (575 °C–650 °C).

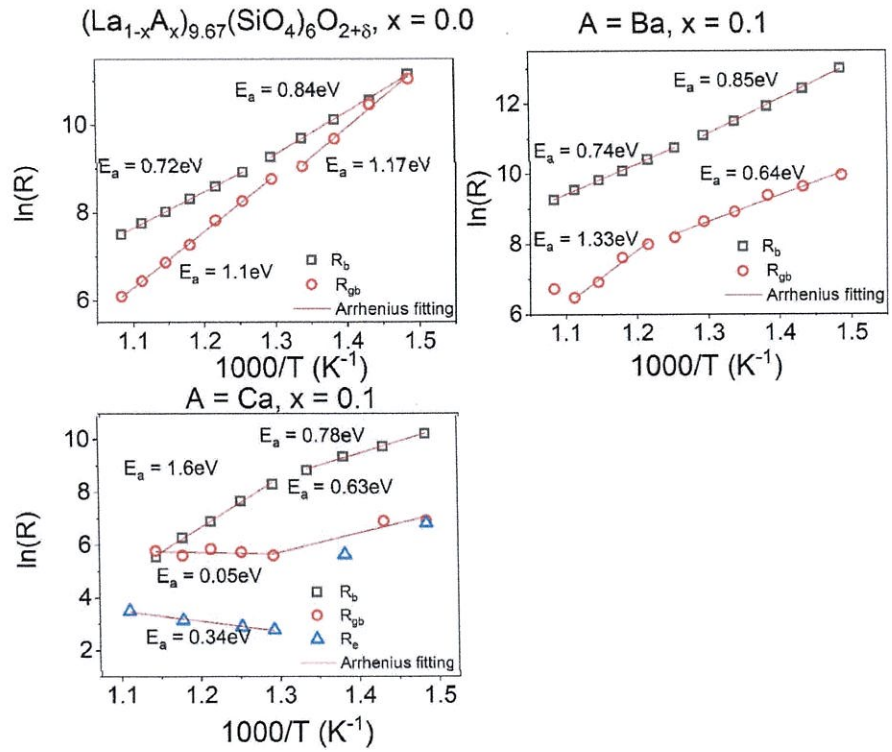

Fig. 12. Arrhenius plots for the grain, grain-boundary and electrode resistances. Here, it is observed again the deviation of fitted lines from the data points. Thus, activation energies are estimated in the two regimes for the $(La_{1-x}A_x)_{9.67}(SiO_4)_6O_{2+\delta}$ system (a) x = 0.0 (b) x = 0.1 with A = Ba, and (c) x = 0.1 with A = Ca.

grain and grain boundary effects. Whereas, in Ca substituted samples, three semicircles in the Nyquist plots are observed for Ca substituted *sample exhibiting grain, grain-boundary and electrode effects. The* grain, grain-boundary and electrode resistances at different temperatures are estimated from the Nyquist or Cole–Cole plots. Fig. 12 depicts the Arrhenius plots for the grain, grain-boundary and electrode *resistances. Here, it is observed again the deviation of fitted lines from* the data points. Thus, activation energies are estimated in the two

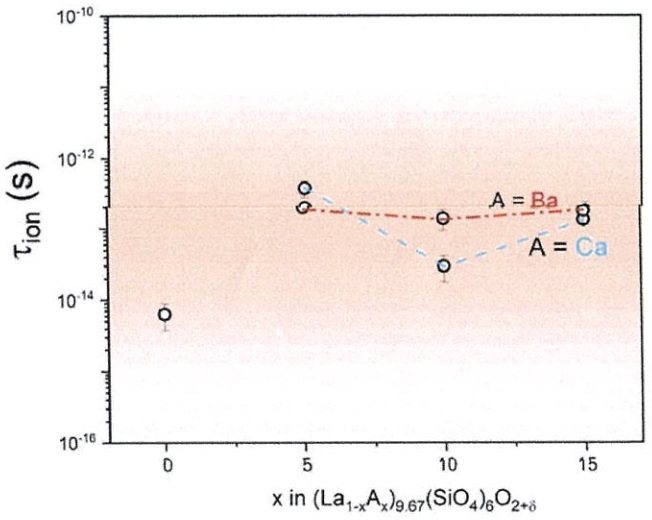

Fig. 13. Variation of mean free ion life time (τ -ion) with content x for Ca and Ba substituted samples.

regimes for the parent, Ba and Ca substituted samples. The two slopes are observed in Arrhenius plots of grain, grain-boundary and electrode resistance. This confirms our earlier observation of two slopes observed in the dc conductivity plots (Fig. 3). Now the slopes can be attributed to the extrinsic contribution at the interface due to the varying charge concentrations at bulk and grain-boundary interfaces (can also be seen through EDX). Moreover, it is also observed that grain, grain boundary and electrode resistances are observed to decrease with increase in temperature manifesting NTCR (negative temperature coefficient of resistance) behaviour.

The mean free ion life time estimated by the probability of transition rate from occupied site to unoccupied site with x is shown in Fig. 13. The data is well fitted with the model showing $\chi^2 > 0.99$ up to 800 K.

$$\frac{1}{\tau} = \frac{1}{\tau_0}\exp\left(-\frac{E_0}{k_B T}\right) \tag{3}$$

The ionic conductivity equation is,

$$\sigma = \frac{1}{3}\left(\frac{(Ze)^2}{k_B T}\right) n_i a_0^2 \omega_0 \, exp(-E_0 / k_B T) \tag{4}$$

Using equations (3) and (4),

$$\frac{\sigma}{\omega} = \frac{1}{3}\left(\frac{(Ze)^2}{k_B T}\right) n_i a_0^2 = \alpha n_i \tag{5}$$

where n_i is number density of ionic species, a_0 is the hopping length. We can see that for x = 0.0, the mean free life time is 10^{-14} s (intramolecular vibration modes) while for the Ca and Ba modified compositions, the mean free ion life time is between 10^{-12} s (intermolecular vibration modes) and 10^{-14} s (intramolecular vibration modes) and 10^{-17} s. It is accounting for the vacancy diffusion mechanism with the formation of polarons due to oxygen deficiency [27].

4. Discussions and concluding remarks

Here, with the ionic radii variation, ion mobility volume has risen to nearly 3 times in Ca substituted sample rather than Ba substituted sample. Moreover, La deficient Ca substituted samples and O deficient Ba substituted samples are obtained. Further, XPS, TGA and Rietveld refinement confirm the formation of La and O deficient Ca and Ba substituted samples, respectively. Moreover, s-p interaction is playing a critical role in the conductivity mechanism of Ca substituted sample. Whereas, loss is occurring due to metal ligand interaction (s-d interaction) in Ba substituted sample. The conductivity, due to connected grain growth increased for x = 0.1 in Ca substituted sample can be attributed to the different local disorder by La vacancy, higher ion mobility volume and s-p interaction. On a comparative note, conductivity reduces in Ba substituted sample due to the decrease in ion mobility volume, creation of O vacancies and s-d interaction.

Fig. 14 (a) shows the variation of percolation energy along the x-axis (PE_X) and z-axis (PE_Z) with $<R_{i,\,La}>$. The vertical solid red line is reference line for x = 0. It can be observed that for lower $<R_{i,\,La}>$ i.e., *Ca* substitution, percolation energy is < 1.5 eV in both the directions. Additionally, both PE_X and PE_Z are particular decreasing with x (at least

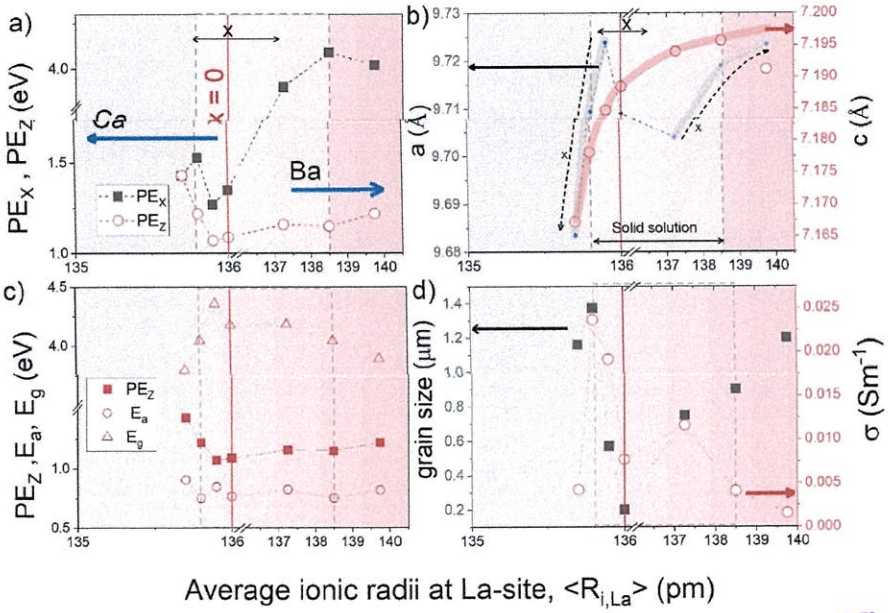

Fig. 14. Variation of (a) percolation energy along the x-axis (PE_X) and z-axis (PE_Z), (b) lattice parameters a and c, (c) PE_Z, activation energy (E_a) and band gap energy (E_g), and (d) grain size and conductivity with average ionic radii at La site $<R_{i,\,La}>$.

with in solubility limits i.e., $x \leq 0.1$ dotted lines). However, in case of materials with greater $<R_{i,\ La}>$ i.e., with Ba substitution, PE_Z shows very small (almost constant) rise with the increase in x. But the interesting feature is observed for PE_X, it is increasing sharply to ~ 4 eV with x. The percolation energy is interrelated to both the structural parameters as well as ion dynamics of materials. Mathematically, it is expressed as $PE = E_a - \beta I(a_o)$, where $I(a_o)$ is energy overlap integral which function of a_o (separation between two donors), β is percolation constant [43]. Recently overlapping large polaron tunnelling is observed for these compounds [44]. Thus, energy overlap integral and hence lattice parameter should be instrumental for understanding the observation of high value of conduction in substituted compounds (in spite of significant lower volume for ion mobility). Fig. 14 (b) shows the variation of lattice parameters 'a' and 'c' with $<R_{i,\ La}>$. A monotonic relation is observed in between lattice parameter c and $<R_{i,\ La}>$. While variation of lattice parameter 'a' is subject to substituents' content but not monotonous with $<R_{i,\ La}>$. This suggests the lattice deformation is significant in a-b plane (concentric hexagons, Fig. 5(b)) while c-axis (O4 channel, Fig. 5(c)) remains almost unaltered. Further, it is also observed in Fig. 14(c) that variation of activation energy, E_a, is almost similar to the variation of PE_Z. However, the band gap energy (Fig. 14(c), estimated from Tauc plots shown in supplementary, Fig. S13) has the opposite trend to that of activation energy and percolation energy along z-axis. This suggests that the conduction should be prominent along O4 channel. It is well known that larger band gap reduces the electronic conductivity and promotes the ionic conductivity. Thus, for the Ca *substituted sample higher band gap is accounted for higher ionic conductivity* instead of Ba substituted samples. This observation is in accordance with the s-p interaction and s-d interaction observed in case of Ca and Ba substituted samples, respectively. Furthermore, grain connectivity also plays a pivotal role in ionic conduction. Thus, the variation of grain size and conductivity with $<R_{i,\ La}>$ are shown in Fig. 14(d). Here, it is observed that within the solid solubility limit, conductivity has the same trend as grain size except for Ba substitution with $x = 0.10$ and $x = 0.15$. Also, the variation of grain size is nearly similar to PE_Z within solubility limit. Hence, it can be summed up as percolation energy, activation energy, band gap, lattice parameter and grain size are controlled via average ionic radii at La site in case of $(La_{1-x}A_x)_{10-\alpha}(SiO_4)_6O_{2+\delta}$ i.e., $PE_z \propto c \propto grain size \propto E_a \propto (1 / E_g) \propto \sigma \propto < R_{i.La} >$.

CRediT authorship contribution statement

Ashishkumar Yadav: Methodology, Formal analysis, Data curation. **Priyanka A. Jha:** Conceptualization, Formal analysis, Visualization, Writing - original draft, Writing - review & editing. **Pardeep K. Jha:** Formal analysis, Writing – review & editing. **Neetu Jha:** Supervision. **Prabhakar Singh:** Supervision, Resources, Funding acquisition, Writing – review & editing.

Declaration of competing interest

The authors declare that they have no known competing financial interests or personal relationships that could have appeared to influence the work reported in this paper.

Data availability

Data will be made available on request.

Acknowledgements

PAJ is thankful to CSIR-SRA (13(9142-A)/2020-pool).

Appendix A. Supplementary data

Supplementary data to this article can be found online at https://doi.org/10.1016/j.matchemphys.2023.127444.

References

[1] K. Kendall, M. Kendall, High-Temperature Solid Oxide Fuel Cells for the 21st Century Fundamentals, Design and Applications, second ed., Elsevier, 2016, ISBN 978-0-12-410453-2.
[2] A.B. Stambouli, E. Traversa, Solid oxide fuel cells (SOFCs): a review of an environmentally clean and efficient source of energy, Renew. Sustain. Energy Rev. 6 (2002) 433–455, https://doi.org/10.1016/S1364-0321(02)00014-X.
[3] Z.Q. Sun, E. Fabbri, L. Bi, E. Traversa, Electrochemical properties and intermediate-temperature fuel cell performance of dense yttrium-doped barium zirconate with calcium addition, J. Am. Ceram. Soc. 95 (2012) 627–635, https://doi.org/10.1111/j.1551-2916.2011.04795.x.
[4] H. Shi, R Ran C Su, J. Cao, Z. Shao, Electrolyte materials for intermediate-temperature solid oxide fuel cells, Prog. Nat. Sci.: Mater. Int. 30 (2020) 764–774, https://doi.org/10.1016/j.pnsc.2020.09.003.
[5] S. Nakayama, T. Kageyama, H. Aono, Y. Sadaoka, Ionic conductivity of lanthanoid silicates, Ln 10 (SiO 4) 6 O 3 (Ln = La, Nd, Sm, Gd, Dy, Y, Ho, Er and Yb), J. Mater. Chem. 5 (1995) 1801–1805, https://doi.org/10.1039/JM9950501801.
[6] H. Okudera, Y. Masubuchi, S. Kikkawa, A. Yoshiasa, Structure of oxide ion-conducting lanthanum oxyapatite, La 9.33 (SiO 4) 6 O 2, Solid State Ionics 176 (2005) 1473–1478, https://doi.org/10.1016/j.ssi.2005.02.014.
[7] B. Ballinger, J. Motuzas, C. Miller, et al., Nanoscale assembly of lanthanum silica with dense and porous interfacial structures, Sci. Rep. 5 (2015) 8210, https://doi.org/10.1038/srep08210.
[8] C. Yamagata, D.R. Elias, M.R.S. Paiva, A.M. Misso, S.R.H. Mello Castanho, Facile preparation of apatite-type lanthanum silicate by a new water-based sol–gel process, Mater. Res. Bull. 48 (2013) 2227–2231, https://doi.org/10.1016/j.materresbull.2013.02.041.
[9] K. Fukuda, T. Asaka, M. Okino, A. Berghout, E. Béchade, O. Masson, I. Julien, P. Thomas, Anisotropy of Oxide-Ion Conduction in Apatite-type Lanthanum silicateSolid State Ionics, vol. 217, 2012, pp. 40–45, https://doi.org/10.1016/j.ssi.2012.04.018.
[10] K. Fukuda, R. Watanabe, M. Oyabu, R. Hasegawa, T. Asaka, H. Yoshida, Oxide-ion conductivity enhancement of polycrystalline lanthanum silicate oxyapatite induced by BaO doping and grain alignment, Cryst. Growth Des. 16 (2016) 4519–4525, https://doi.org/10.1021/acs.cgd.6b00638.
[11] S.W. Tao, J.T.S. Irvine, Preparation and characterisation of apatite-type lanthanum silicates by a sol-gel process, Mater. Res. Bull. 36 (2001) 1245–1258, https://doi.org/10.1016/S0025-5408(01)00625-0.
[12] L.L. León-Reina, E.R. Losilla, M. Martínez-Lara, S. Bruque, M.A.G. Aranda, Interstitial oxygen conduction in lanthanum oxy-apatite electrolytes, J. Mater. Chem. 14 (2004) 1142, https://doi.org/10.1039/B315257J.
[13] S.S. Pramana, W.T. Klooster, T.J. White, Framework 'interstitial' oxygen in La 10 (GeO 4) 5 (GeO 5)O 2 apatite electrolyte, Acta Crystallogr., Sect. B: Struct. Sci. 63 (2007) 597–602.
[14] Y. Matsushita, F. Izumi, K. Kobayashi, N. Igawa, H. Kitazawa, Y. Oyama, S. Miyoshi, S. Yamaguchi, Powder neutron diffraction of La-apatite under low temperature, Nucl. Instrum. Methods Phys. Res., Sect. A 600 (2009) 319–321, https://doi.org/10.1016/j.nima.2008.11.081.
[15] J. Felsche, Rare earth silicates with the apatite structure, J. Solid State Chem. 5 (1972) 266–275, https://doi.org/10.1016/0022-4596(72)90039-4.
[16] S. Lambert, A. Vincent, E. Bruneton, S. Beaudet-Savignat, F. Guillet, B. Minot, F. Bouree, Structural investigation of La 9.33 Si 6 O 26- and La 9 AESi 6 O 26+δ -doped apatites-type lanthanum silicate (AE=Ba, Sr and Ca) by neutron powder diffraction, J. Solid State Chem. 79 (2006) 2602–2608.
[17] S. Guillot, S. Beaudet-Savignat, S. Lambert, R.-N. Vannier, P. Roussel, F. Porcher, Evidence of local defects in the oxygen excess apatite La 9.67 (SiO 4) 6 O 2.5 from high resolution neutron powder diffraction, J. Solid State Chem. 182 (2009) 3358–3364.
[18] S. Nakayama, M. Sakamoto, M. Higuchi, K. Kodaira, M. Sato, S. Kakita, T. Suzuki, K. Itoh, Oxide ionic conductivity of apatite type Nd 9·33 (SiO 4) 6 O 2 single crystal, J. Eur. Ceram. Soc. 19 (1999) 507–510, https://doi.org/10.1016/S0955-2219(98)00215-5.
[19] J.E.H. Sansom, D. Richings, P.R. Slater, A powder neutron diffraction study of the oxide-ion-conducting apatite-type phases, La 9.33 Si 6 O 26 and La 8 Sr 2 Si 6 O 26, Solid State Ionics 139 (2001) 205–210, https://doi.org/10.1016/S0167-2738(00)00835-3.
[20] S. Ide, H. Takahashi, I. Yashima, K. Suematsu, K. Watanabe, K. Shimanoe, Effect of boron substitution on oxide-ion conduction in c-axis-oriented apatite-type lanthanum silicate, J. Phys. Chem. C 124 (2020) 2879–2885, https://doi.org/10.1021/acs.jpcc.9b11454.
[21] A. Vincent, S. Beaudet-Savignat, F. Gervais Bruneton, Elaboration and ionic conduction of apatite-type lanthanum silicates doped with Ba, La 10−x Ba x (SiO 4) 6 O 3−x/2 with x = 0.25–2, J. Eur. Ceram. Soc. 27 (2007) 1187–1192, https://doi.org/10.1016/j.jeurceramsoc.2006.05.090.
[22] C.Y. Ma, P. Briois, J. Böhlmark, F. Lapostolle, A. Billard, La 9.33 Si 6 O 26 electrolyte thin films for IT-SOFC application deposited by a HIPIMS/DC hybrid magnetron sputtering process, Ionics 14 (2008) 471–476, https://doi.org/10.1007/s11581-008-0239-7.

[23] J.E.H. Sansom, A. Najib, P.R. Slater, Oxide ion conductivity in mixed Si/Ge-based apatite-type systems, Solid State Ionics 175 (2004) 353–355, https://doi.org/10.1016/j.ssi.2003.12.030.
[24] C. Bonhomme, S. Beaudet-Savignat, T. Chartier, A. Maître, A.L. Sauvet, B. Soulestin, Sintering kinetics and oxide ion conduction in Sr-doped apatite-type lanthanum silicates, La 9 Sr 1 Si 6 O 26.5, Solid State Ionics 180 (2009) 1593–1598, https://doi.org/10.1016/j.ssi.2009.10.009.
[25] K. Kobayashi, Y. Sakka, Research progress in nondoped lanthanoid silicate oxyapatites as new oxygen-ion conductors, J. Ceram. Soc. Jpn. 122 (2014) 921–939, https://doi.org/10.2109/jcersj2.122.921.
[26] O.N. Verma, P.K. Jha, P. Singh, A structural-electrical property correlation in A-site double substituted lanthanum aluminate, J. Appl. Phys. 122 (2017), 225106, https://doi.org/10.1063/1.4999002.
[27] O.N. Verma, P.A. Jha, P. Singh, P.K. Jha, P. Singh, Influence of iso-valent 'Sm' double substitution on the ionic conductivity of La 0.9 Sr 0.1 Al 0.9 Mg 0.1 O 3-δ ceramic system, Mater. Chem. Phys. 241 (2020), 122345, https://doi.org/10.1016/j.matchemphys.2019.122345.
[28] H. Yoshioka, Enhancement of ionic conductivity of apatite-type lanthanum silicates doped with cations, J. Am. Ceram. Soc. 90 (2007) 3099–3105, https://doi.org/10.1111/j.1551-2916.2007.01862.x.
[29] H. Yoshioka, Y. Nojiri, S. Tanase, Ionic conductivity and fuel cell properties of apatite-type lanthanum silicates doped with Mg and containing excess oxide ions, *Solid State Ionics 179 (2008) 2165–2169, https://doi.org/10.1016/j.ssi.2008.07.022.*
[30] Y. Nojiri, S. Tanase, M. Iwasa, H. Yoshioka, Y. Matsumura, T. Sakai, Ionic conductivity of apatite-type solid electrolyte material, La 10−X Ba X Si 6 O 27−X/2 (X = 0–1), and its fuel cell performance, J. Power Sources 195 (2010) 4059–4064, https://doi.org/10.1016/j.jpowsour.2010.01.050.
[31] S. Beaudet-Savignat, A. Vincent, S. Lambert, F. Gervai, Oxide ion conduction in Ba, Ca and Sr doped apatite-type lanthanum silicates, J. Mater. Chem. 17 (2007) 2078–2087, https://doi.org/10.1039/B615104C.
[32] Y. Ogura, T. Yokoi, K. Fujii, M. Yashima, K. Matsunaga, First-principles analysis of the oxide-ion conduction mechanism in Si-deficient lanthanum silicate apatite, J. Phys. Chem. C 126 (2022) 5805–5812, https://doi.org/10.1021/acs.jpcc.1c10486.
[33] A.K. Jonscher, Dielectric Relaxation in Solids, Chelsea Dielectrics Press, London, 1983.
[34] P.K. Jha, P.A. Jha, V. Singh, P. Kumar, K. Asokan, R.K. Dwivedi, Diffuse phase ferroelectric vs. Polomska transition in (1-x) BiFeO 3 -(x) Ba Zr 0.025 Ti 0.975 O 3 ($0.1 \leq x \leq 0.3$) solid solutions, J. Appl. Phys. 117 (3) (2015), 024102, https://doi.org/10.1063/1.4905715.
[35] B.I. Shklovskii, A.L. Efros, in: M. Cardona (Ed.), Electronic Properties of Doped Semiconductors, Springer, Berlin, 1984.
[36] D.N. Trong, V.C. Long, Ş. Talu, U. Sarac, P.N. Dang, K.P. Huu, A new study on the structure, and phase transition temperature of bulk silicate materials by simulation method of molecular dynamics, J. Compos. Sci. 6 (2022) 234, https://doi.org/10.3390/jcs6080234.
[37] F.X. Zhang, M. Lang, J.M. Zhang, Z.Q. Cheng, Z.X. Liu, J. Lian, R.C. Ewing, Phase transition and abnormal compressibility of lanthanide silicate with the apatite structure, Phys. Rev. B 85 (2012), 214116, https://doi.org/10.1103/PhysRevB.85.214116.
[38] M.W. Barsoum, Fundamentals of Ceramics, IOP publishing, 2007.
[39] D. Kumar, A.S. Bangwal, S. Singh, P.A. Jha, P. Singh, High –temperature conduction mechanism of samarium ferrite substituted sodium niobate ceramics, Phys. B Condens. Matter 582 (2020), 412028, https://doi.org/10.1016/j.physb.2020.412028.
[40] T. Liao, T. Sasaki, Z. Sun, The oxygen migration in the apatite-type lanthanum *silicate with the cation substitution, Phys. Chem. Chem. Phys. 15 (2013), 17553,* https://doi.org/10.1039/c3cp52245h.
[41] S. Singh, M. Kumar, P.K. Jha, P.A. Jha, P. Singh, Observation of grey cesium tin bromide with unusual phase transition, EPL 141 (2023), 26001, https://doi.org/10.1209/0295-5075/acab7f.
[42] P.C. Bharti, P.K. Jha, P.A. Jha, P. Singh, Observation of isomorphic phase transition in non-perovskite Green CsSnI 3, Materialia 27 (2023), 101646, https://doi.org/10.1016/j.mtla.2022.101646.
[43] S. Abboudy, A quasi-universal percolation approach of hopping activation energy and metal-nonmetal transition in semiconductors, Physica B 212 (1995) 175–180, https://doi.org/10.1016/0921-4526(95)00012-X, 1995.
[44] A.K. Yadav, P.A. Jha, P.K. Jha, N. Jha, P. Singh, Overlapping large polaron tunnelling in lanthanum silicate oxyapatite, J. Phys. Condens. Matter 35 (2023), 095702, https://doi.org/10.1088/1361-648X/acad53, 09.